

Strain tunable anomalous Hall and Nernst conductivities in compensated ferrimagnetic Mn_3Al

Guihyun Han¹, Minkyu Park^{1,2,*} and S. H. Rhim^{1†}

¹ Department of Physics, University of Ulsan, 93, Dachak-ro, Nam-gu, Ulsan, Republic of Korea

² Quantum Technology Institute, Korea Research Institute of Standards and Science, 267, Gajeong-ro, Yuseong-gu, Daejeon, Republic of Korea

The tunability of anomalous Hall and Nernst conductivities is investigated in the compensated ferrimagnet Mn_3Al under isotropic strain (η) and chemical potential variation using first-principles calculations. At a chemical potential of $\mu = -0.3$ eV, three distinct topological features—Weyl points, nodal lines, and gapped nodal lines—are simultaneously realized along high-symmetry directions of the Brillouin zone in the framework of magnetic space group. The anomalous Hall conductivity (AHC) is found to be predominantly governed by the Berry curvature in the $k_y k_z$ plane and can be enhanced significantly under tensile strain, reaching -1200 $(\Omega \text{ cm})^{-1}$. On the other hand, the anomalous Nernst conductivity (ANC) shows a sign change near the Fermi level and whose magnitude increases at $\mu = -0.3$ eV with quasi-quadratic strain dependence. Regardless of strain, the underlying bands and Fermi surface structures remain robust, while the distribution and magnitude of Berry curvature evolve substantially. These results underscore the potential of Mn_3Al , a compensated ferrimagnet, as a platform for Berry curvature engineering via strain and doping.

I. INTRODUCTION

In modern spintronics, the role of the anomalous Hall effect (AHE) and anomalous Nernst effect (ANE) are increasing, by providing an efficient mechanism to generate transverse charge and spin current without relying on external magnetic fields[1–3]. Both AHE and ANE arise from the interplay of topology of electronic structure, spin-orbit coupling, and broken time-reversal symmetry [4–8]. The intrinsic origins of AHE and ANE are now widely understood in terms of the Berry curvature of electronic bands, with topological features such as Weyl points and nodal lines playing crucial roles[4, 9, 10].

In recent years, compensated ferrimagnets and some antiferromagnets, with vanishing net magnetization, have emerged as promising hosts of large AHE and ANE, combining broken time-reversal symmetry with vanishing net magnetization[6, 8, 11–15]. The vanishing net magnetization is advantageous for overcoming stray fields while still supporting a robust Berry curvature. In particular, Heusler compounds are versatile owing to tunable crystal structures, rich magnetic phase diagrams, and compatibility with spintronic technologies[16–18]. Such flexibility makes Heusler compounds excellent platforms for studying and engineering topological transport properties.

A representative example is Mn_3Al , a compensated collinear ferrimagnet in a cubic Heusler, with half-metallicity and Curie temperature of 605 K[19]. The magnetic symmetry of Mn_3Al allows a nonzero anomalous Hall conductivity despite zero net magnetization[20, 21]. Previous studies have identified its intrinsic AHE, associated with symmetry-protected Berry curvature hot

spots[20]. However, how this anomalous response evolves under external tuning—such as isotropic strain or chemical potential variation—has not been fully clarified. Moreover, the possible coexistence of multiple topological features under such conditions has remained unexplored.

In this work, we employ first-principles calculations to reveal that Mn_3Al simultaneously hosts Weyl points, nodal lines, and gapped nodal lines around a chemical potential of $\mu = -0.3$ eV, located along high-symmetry directions of its magnetic Brillouin zone. These topological features give rise to strongly strain-dependent variations in both anomalous Hall and Nernst conductivities. Our findings suggest that compensated Heusler ferrimagnets provide a promising route for Berry-curvature engineering of spintronic devices[22–31]. Such engineering has already been demonstrated under hydrostatic pressure [27–29] and via chemical potential variation [30, 31].

II. STRUCTURE AND MAGNETIC SPACE GROUP

Crystal structure of a regular Heusler compound, Mn_3Al , in $D0_3$ structure is depicted in Fig. 1 (a), whose space group is $Fm\bar{3}m$ (No. 225). It can be viewed as a superposition of two fcc of Al and Mn(I) with Mn(II) locating at the center of cubic box formed by Mn(I) and Al (denoted by green lines). Site symmetry of constituent atoms are $m\bar{3}m(4a)$ for Al, $m\bar{3}m(4b)$ for Mn(I), and $\bar{4}3m(8c)$ for Mn(II), respectively. Different site symmetry results in distinct magnetic moments of Mn(I) and Mn(II). While Al has negligible moment, moment of Mn(I) is $2.6\mu_B$ and that of Mn(II) is $-1.3\mu_B$, respectively.

Brillouin zone of Mn_3Al is shown in Fig. 1 (b) with labels for high symmetry points. For $Fm\bar{3}m$, high-symmetry points shown in blue (M, S, G) and red

* minkyupark@kriss.re.kr

† sonny@ulsan.ac.kr

(X, U, P) are equivalent. They are inequivalent in the presence of magnetization along z axis, whose magnetic space group is $I4/mm'm'$ (No. 139.537). Under 4-fold rotation along z axis, 4_{001} , the crystal structure is invariant. On the other hand, the fourfold rotation 4_{100} around the x axis leaves the chemical structure invariant but alters the magnetic structure. Hence, 4_{001} is the symmetry operation of magnetic space group, $I4/mm'm'$ (No. 139.537), but 4_{100} is not. In this context, $\Gamma - M$ has 4-fold rotational symmetry while $\Gamma - X$ has no such in $I4/mm'm'$ (No. 139.537).

III. METHODS OF CALCULATIONS

First-principles calculations are performed using Vienna *ab initio* simulation package (VASP) with spin-orbit coupling included[32]. For the exchange-correlation energy, generalized gradient approximation (GGA) is used with Perdew-Burke-Ernzerhof (PBE) parameterization [33]. Summation in Brillouin zone is done with $15 \times 15 \times 15$ k grid. Cutoff energy for wave function expansion is 450 eV. Optimized lattice constant is 5.78 Å in good agreement with experiment [19].

After self-consistent calculations, maximally-localized Wannier functions (MLWFs) are obtained using Wannier90 [34, 35] with $9 \times 9 \times 9$ k grid. The initial projections were chosen using d orbitals for Mn and s and p for Al atoms. 38 maximally-localized Wannier functions (MLWFs) are constructed from 72 Bloch bands. Berry curvature is computed using WannierBerri [36] via Wannier interpolation with $300 \times 300 \times 300$ k grid.

Anomalous Hall conductivity (AHC) is obtained by summing up Berry curvature, $\Omega_{n,\alpha\beta}(\mathbf{k})$, over occupied states in Brillouin zone[11],

$$\sigma_{\alpha\beta} = \frac{e^2}{\hbar} \int \frac{d^3k}{(2\pi)^3} \sum_n f_{n\mathbf{k}} \Omega_{n,\alpha\beta}(\mathbf{k}), \quad (1)$$

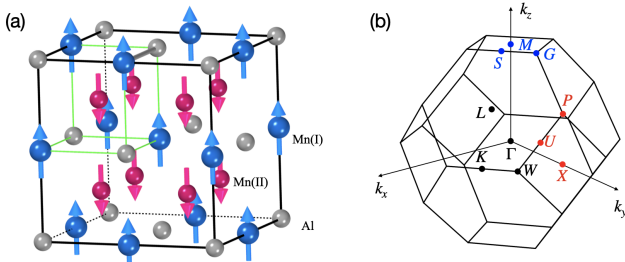


FIG. 1. (a) Crystal structure of Mn₃Al with magnetization along [001]. Mn(I), Mn(II), and Al are in blue, red, and gray spheres, respectively, with magnetic moments shown in arrows. Green line denotes cube formed by Mn(I) and Al, where Mn(II) is at the center of the cube. (b) Brillouin zone of Mn₃Al of magnetic space group $I4/mm'm'$ (No. 139.537). High symmetry points, symmetrically equivalent in space group but distinct in magnetic space group, are distinguished by colors.

where e is the elementary charge; $f_{n\mathbf{k}}$ is the Fermi-Dirac distribution of n -th band of k . The Berry curvature is obtained from Kubo formula,

$$\Omega_{\alpha\beta}(\mathbf{k}) = - \sum_{n \neq n'} \frac{2\text{Im} [\langle n\mathbf{k} | \mathbf{v}_\alpha | n'\mathbf{k} \rangle \langle n'\mathbf{k} | \mathbf{v}_\beta | n\mathbf{k} \rangle]}{(\varepsilon_{n\mathbf{k}} - \varepsilon_{n'\mathbf{k}})^2}, \quad (2)$$

where \mathbf{v}_α is the velocity operator of α -th component; $\varepsilon_{n\mathbf{k}}$ is energy of n -th band of k .

Anomalous Nernst conductivity (ANC) is expressed in terms of Berry curvature[9],

$$\alpha_{\alpha\beta} = \frac{e}{\hbar} \int \frac{d^3k}{(2\pi)^3} \sum_n S_n(\mathbf{k}) \Omega_{n,\alpha\beta}(\mathbf{k}). \quad (3)$$

Here $S_n(\mathbf{k})$ is the entropy of fermion,

$$S_n(\mathbf{k}) = -k_B [f_{n\mathbf{k}} \log f_{n\mathbf{k}} + (1 - f_{n\mathbf{k}}) \log (1 - f_{n\mathbf{k}})], \quad (4)$$

where k_B is the Boltzmann constant. In the low temperature limit, ANC is commonly expressed by Mott relation, $\alpha_{\alpha\beta} = (\pi^2/3)(k_B^2 T/e) \lim_{T \rightarrow 0} \partial \sigma_{\alpha\beta} / \partial \mu$. This limit represents the Berry curvature contribution on the Fermi surface[9, 20].

IV. RESULTS AND DISCUSSIONS

A. Band crossing and Nodal line

Band structure of Mn₃Al without strain is shown in Fig. 2. Red (blue) of bands represent the amplitude of k resolved Berry curvature with positive (negative) sign. In Fig. 2 (a), color-labeled high symmetry points are classified as crossing, Weyl points, and avoided crossing, respectively. Mn₃Al is half-metallic with band gap 0.4 eV in the minority spin channel. This half-metallicity is robust with strain [37]. Around Γ , large Ω emerges with alternating signs. More dominant Ω is evident near L : while bands around $E_F - 0.2$ eV have both signs, rather dispersive band crossing around E_F has large contribution. Ω around M has also pronounced contribution near E_F with both signs.

Fig. 2 (b-c) show enlarged views of colored boxes of Fig. 2 (a). Brillouin zone with (001) and (100) plane are shown respectively, which contain k paths of our interest. Band analysis along $X - W$ is shown in Fig. 2 (b); that along $X - P$ and $G - M$ is in Fig. 2 (c). Little groups with corresponding representations are on top along color-coded Berry curvature.

Along $X - W$, band crossing of XW_3 and XW_4 states are evident, where (001) is the mirror plane containing $X - W$. Along $X - P$, the band crossing of XP_3 and XP_4 is Weyl point, where (100) is not a mirror plane when the magnetization is along (001). On the other hand, the path along $G - M$, the (100) plane not being a mirror plane results in avoided crossing of GM_3 and GM_4 , where positive and negative Berry curvature is apparent above

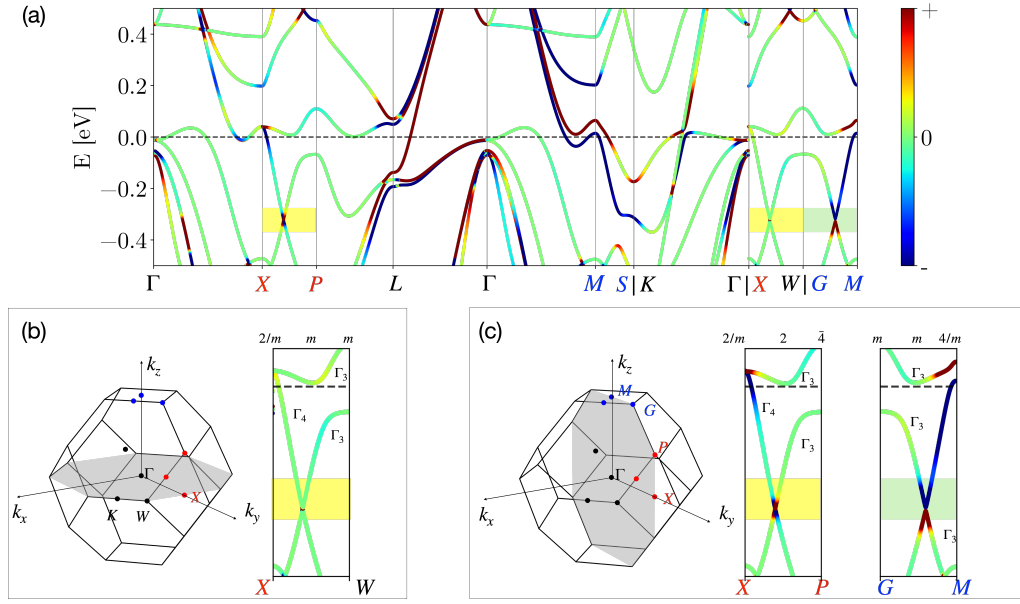


FIG. 2. (a) k projected Berry curvature of Mn_3Al without strain. Symmetrically distinct k points are distinguished by colors in black, blue, and red. Shade boxes denote: crossing (in yellow) and avoided crossing (in blue). Crossing are further classified into crossing and Weyl points (see text). (b) (001) plane in Brillouin zone containing $X-W$, where crossing is denoted in yellow box. (c) (100) plane in Brillouin zone containing $X-P$ and $G-M$, which are Weyl point and avoided crossing, respectively. In insets of (b) and (c), group of k and representation of bands are shown, where color of bands are k resolved Berry curvature.

and below the gap. From this symmetry analysis, Mn_3Al contains band crossing, Weyl point, and avoided crossing when $\mu = E_F - 0.3 eV [38].$

B. Anomalous Hall and Nernst Conductivity

Fig. 3 presents the anomalous Hall (σ_{xy}) and the Nernst conductivity (α_{xy}). In Fig. 3 (a-b), σ_{xy} and α_{xy} are presented as function of strain (η) and the chemical potential (μ) in color contour, where bright color correspond large $|\Omega|$. Solid (dashed) lines denote $\mu = E_F$ ($\mu = E_F - 0.3$ eV), where $T = 100 K is used. For σ_{xy} , bright yellow region appears for $\eta = -5\%$ just above $\mu = E_F$, which rather monotonically shifts to positive strain with $\mu < E_F$. Bright area is most pronounced for positive strains when $E_F - 0.3 < \mu < E_F - 0.1 eV.$$

For α_{xy} , positive (negative) values are denoted by red (blue) colors. As seen, when $\mu = E_F$, both positive and negative α_{xy} appear with strain. Without strain $\sigma_{xy} = 670 ($\Omega \text{ cm}$) $^{-1}$, which becomes largest with $830 ($\Omega \text{ cm}$) $^{-1}$ for $\eta = -2\%$; while α_{xy} around $\mu = E_F - 0.3$ eV is large around 2.92 (A/K m) with negative sign.$$

To reveal clear strain dependence, σ_{xy} and α_{xy} are plotted in Fig. 3 (c-d) as function of strain, for two chemical potentials, $\mu = E_F$ and $\mu = E_F - 0.3$ eV, denoted by solid and open symbols, respectively. First, AHC is plotted in Fig. 3 (c). When $\mu = E_F$, σ_{xy} is in the range of $-1200 \sim -300 ($\Omega \text{ cm}$) $^{-1}$. For $\eta = +2\%$, σ_{xy} is largest with $-800 ($\Omega \text{ cm}$) $^{-1}$. When $\mu = E_F - 0.3$ eV, on the other hand, σ_{xy} exhibits clear tendency of mono-$$

tonic decrease, or increase of magnitude, which reaches as high as $-1100 ($\Omega \text{ cm}$) $^{-1}$ for $\eta = +5\%$. Second, ANC is plotted in Fig. 3 (d). When $\mu = E_F$, α_{xy} is negative for compressive strain turning positive for $\eta = -2\%$. It becomes negative for $\eta > +3\%$. α_{xy} reaches 2.17 and$

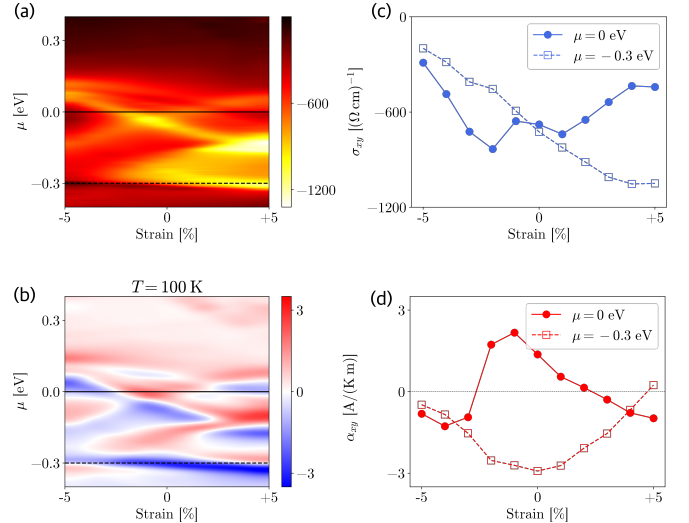


FIG. 3. (a) Anomalous Hall conductivity (σ_{xy}) and (b) anomalous Nernst conductivity (α_{xy}) as function of strain and chemical potential in color contour. Solid and dashed lines correspond to $\mu = E_F$ and $\mu = E_F - 0.3$ eV, respectively. (c) σ_{xy} and (d) α_{xy} with respect to strain for $\mu = E_F$ (solid line with filled symbol) and $\mu = E_F - 0.3$ eV (dashed line with open symbols), respectively.

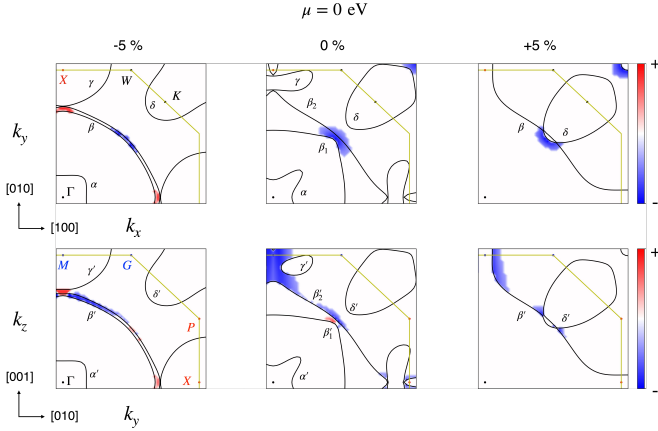


FIG. 4. Contour of Berry curvature when $\mu = E_F$ for $\eta = -5$, 0, and $+5\%$ from left to right column. Upper panel: $\Omega_{xy}(\mathbf{k})$ on $k_x k_y$ plane (001) and lower panel: contour on $k_y k_z$ plane (100). Red (blue) color denotes positive (negative) $\Omega_{xy}(\mathbf{k})$. Yellow line is for Brillouin zone boundary. Fermi surface is shown in black lines, where individual Fermi sheets are labeled by α , β , γ , and δ . High symmetry point labeled in black, red, and blue are consistent with Fig. 2.

1.73 (A/K m) for $\eta = 0\%$ and $\eta = -1\%$. The sign change of α , as expressed in Eq.3, is a manifest of sign of over all Berry curvature with strain. When $\mu = E_F - 0.3$ eV, α_{xy} exhibits quasi-quadratic feature with local minimum -2.92 (A/K m) near zero strain [39].

C. Fermiology: $\mu = E_F$ and $\mu = E_F - 0.3$ eV

As discussed earlier, AHC and ANC exhibit differently for $\mu = E_F$ and $\mu = E_F - 0.3$ eV. When $\mu = E_F$, the Berry curvature is maximized without strain both on $k_x k_y$ and $k_y k_z$ planes. With compressive strain, the magnitude of AHC is reduced with positive Berry curvature. With tensile strain, AHC is reduced with the smaller magnitude of Berry curvature in narrow region. When $\mu = E_F - 0.3$ eV, Berry curvature is dominantly from $k_y k_z$ plane. The magnitude of Berry curvature increases with strain. Here, the evolution of Fermi surface (FS) with respect to strain is discussed with concomitant distribution of Berry curvature for each μ . Fig. 4 and Fig. 5 show Berry curvature distribution with FS contour on $k_x k_y$ and $k_y k_z$ planes, whose bands structures are presented in Fig. 2 (b) and (c). With SOC, FS on $k_x k_y$ and $k_y k_z$ planes are quite similar but different, which are equivalent without SOC. FS sheets are labelled as α , β , γ , and δ for $\mu = E_F$. Primes are used to for contours when $\mu = E_F - 0.3$ eV. In the following, aforementioned discussion is presented for $\eta = -5$, 0, and $+5\%$. Cases for other strains are shown in Supplemental Material [40].

$\mu = E_F$: Contour of FS on $k_x k_y$ and $k_y k_z$ planes are almost the same except for γ with $\eta = 0\%$. α is evident for $\eta = -5\%$ and $\eta = 0\%$, which disappears for $\eta = +5\%$.

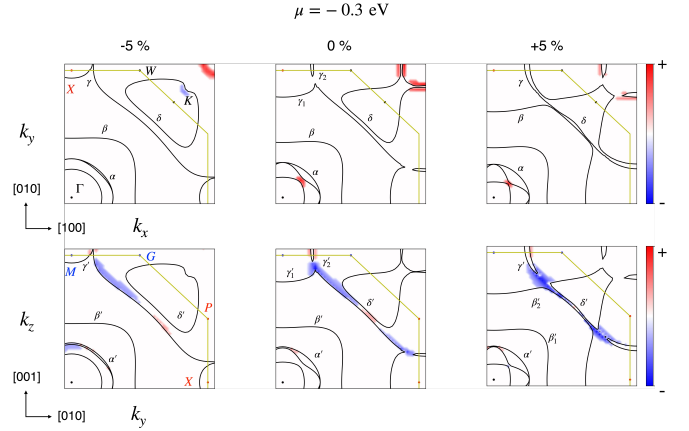


FIG. 5. Contour of Berry curvature when $\mu = E_F - 0.3$ eV for $\eta = -5$, 0, and $+5\%$. Upper panel: $\Omega_{xy}(\mathbf{k})$ near the $k_x k_y$ plane (001) and lower panel: contour on $k_y k_z$ plane (100). Red (blue) color denotes positive (negative) $\Omega_{xy}(\mathbf{k})$. Yellow line is for Brillouin zone boundary. Fermi surface is shown in black lines, where individual Fermi sheets are labeled by α' , β' , γ' , and δ' . High symmetry point labelled in black, red, and blue are consistent with Fig. 2.

β for $\eta = -5\%$ is in arc-shape with nearly two identical bands. For $\eta = 0\%$, β is composed of two pieces, denoted as β_1 and β_2 , while for $\eta = +5\%$ it is a single piece. Ellipse-shaped δ around K , with increasing strain, shifts toward the β , which intersects β for $\eta = +5\%$. A notable difference between the $k_x k_y$ and $k_y k_z$ planes is prominent in γ sheet for $\eta = 0\%$. On $k_x k_y$ plane, γ is nearly circular arc shape for $\eta = -5\%$ and elongated for $\eta = 0\%$, it disappears for $\eta = +5\%$. However, on $k_y k_z$ plane, γ is closed contour near M for $\eta = 0\%$.

While FS on $k_x k_y$ and $k_y k_z$ planes look similar, the Berry curvature distributions differ significantly. On $k_x k_y$ plane, α has no appreciable Ω with and without strain. For $\eta = -5\%$, β has $\Omega > 0$ around k_x and k_y axis and $\Omega < 0$ around $\frac{1}{2}\Gamma K$. For $\eta = 0\%$, β_1 and β_2 have large $\Omega < 0$ around $\frac{1}{2}\Gamma K$. For $\eta = +5\%$, β and δ have large Ω around $\frac{1}{2}\Gamma K$. On $k_y k_z$ plane, α still has no contribution with and without strain. For $\eta = -5\%$, β has both signs of Ω . $\Omega < 0$ appears around k_y and k_z axis while $\Omega > 0$ does near k_z axis. For $\eta = 0\%$, both $\Omega > 0$ and $\Omega < 0$ emerge near $\frac{1}{2}MX$ where nearly degenerate bands are retained and $\Omega < 0$ is pronounced in large region outside γ . For $\eta = +5\%$, β is single-banded with appreciable $\Omega < 0$ around crossing with δ and arc close to k_z axis.

$\mu = E_F - 0.3$ eV: The Fermiology, at first sight, is quite similar for all strains [41]. On $k_x k_y$ plane for $\eta = -5\%$, α' is also four-fold but the degeneracy is lifted along $\Gamma - K$. β' is rather straight line further away from Γ with respect to $\mu = E_F$. γ' around X is similar to $\mu = E_F$ with smaller size. δ' around K is oval-shaped with little distortion. For $\eta = 0\%$, while the overall Fermiology is retained respect to $\eta = -5\%$, the details need some comments. The lifted degeneracy of α' is larger (smaller)

than compressive (tensile) along $\Gamma - K$. γ' is split into γ'_1 and γ'_2 . δ' is smaller. For $\eta = +5\%$, α' is almost the same as the case for $\eta = 0\%$. γ'_1 , γ'_2 , and δ' is getting closer and γ'_2 is collapsed to δ' . On $k_y k_z$ plane, the Fermiology is remains the same as on $k_x k_y$ plane except for $\eta = +5\%$. γ'_1 , γ'_2 , and δ' is getting closer similar to $k_y k_z$, but not collapsed.

Now, we move on to Berry curvature distribution. On $k_x k_y$ plane, for $\eta = -5\%$, there is no big contribution of Ω . For $\eta = 0$ and $+5\%$, $\Omega > 0$ appears along $\Gamma - K$. On $k_y k_z$ plane, for $\eta = -5\%$, $\Omega < 0$ appears near α' and γ' . For $\eta = 0$ and $+5\%$, $\Omega < 0$ contribution are found near γ'_1 , γ'_2 , and δ' , differing in their magnitudes. Similar distribution but only the magnitude differences are found for other strains [42].

V. CONCLUSION

We have investigated the anomalous Hall conductivity (AHC) and anomalous Nernst conductivity (ANC) of the compensated ferrimagnet Mn_3Al under isotropic strain and chemical potential variation, based on first-principles calculations. When $\mu = -0.3$ eV, three distinct topological features—Weyl points, nodal lines, and gapped nodal lines—are simultaneously realized, occurring along distinct high-symmetry directions in the Bril-

louin zone in the framework of magnetic space group. These symmetry-protected features govern the Berry curvature landscape and strongly influence transverse transport. Dominant contribution to AHC arises from the $k_y k_z$ plane; the isotropic strain can significantly enhance AHC, reaching up to -1200 ($\Omega \text{ cm}$) $^{-1}$. Meanwhile, ANC shows a sign reversal near the Fermi level and becomes strongly negative at $\mu = -0.3$ eV for all strains except $\eta = +5\%$. While the overall band structure and Fermi surface topology are retained under strain, the Berry curvature magnitude and distribution evolve markedly. These results demonstrate how the interplay of symmetry, topology, and tunable parameters such as strain and doping interplay influences transverse transport responses in Mn_3Al , highlighting its potential as a model system for strain-engineered spintronic applications and Berry curvature-driven transport phenomena.

ACKNOWLEDGMENTS

This research is supported by National Research Foundation (NRF) of Korea (NRF-RS-2022-NR068225 and NRF-RS-2024-00449996). We are also grateful for support by the National Supercomputing Center with supercomputing resources (KSC-2025-CRE-0016) and computational resource of the UNIST Supercomputing center.

[1] S. Nakatsuji, N. Kiyohara, and T. Higo, Large anomalous Hall effect in a non-collinear antiferromagnet at room temperature, *Nature* **527**, 212 (2015).

[2] M. Kimata, H. Chen, K. Kondou, S. Sugimoto, P. K. Muduli, M. Ikhlas, Y. Omori, T. Tomita, A. H. MacDonald, S. Nakatsuji, and Y. Otani, Magnetic and magnetic inverse spin Hall effects in a non-collinear antiferromagnet, *Nature* **565**, 627 (2019).

[3] K. Uchida, S. Takahashi, K. Harii, J. Ieda, W. Koshibae, K. Ando, S. Maekawa, and E. Saitoh, Observation of the spin Seebeck effect, *Nature* **455**, 778 (2008).

[4] N. Nagaosa, J. Sinova, S. Onoda, A. H. MacDonald, and N. P. Ong, Anomalous Hall effect, *Rev. Mod. Phys.* **82**, 1539 (2010).

[5] H. Chen, Q. Niu, and A. H. MacDonald, Anomalous Hall Effect Arising from Noncollinear Antiferromagnetism, *Phys. Rev. Lett.* **112**, 017205 (2014).

[6] J. Kübler and C. Felser, Non-collinear antiferromagnets and the anomalous Hall effect, *Europhys. Lett.* **108**, 67001 (2014).

[7] T. Jungwirth, Q. Niu, and A. H. MacDonald, Anomalous Hall Effect in Ferromagnetic Semiconductors, *Phys. Rev. Lett.* **88**, 207208 (2002).

[8] L. Šmejkal, A. B. Hellenes, R. González-Hernández, J. Sinova, and T. Jungwirth, Giant and Tunneling Magnetoresistance in Unconventional Collinear Antiferromagnets with Nonrelativistic Spin-Momentum Coupling, *Phys. Rev. X* **12**, 011028 (2022).

[9] D. Xiao, Y. Yao, Z. Fang, and Q. Niu, Berry-Phase Effect in Anomalous Thermoelectric Transport, *Phys. Rev. Lett.* **97**, 026603 (2006).

[10] D. Xiao, M.-C. Chang, and Q. Niu, Berry phase effects on electronic properties, *Rev. Mod. Phys.* **82**, 1959 (2010).

[11] Y. Yao, L. Kleinman, A. H. MacDonald, J. Sinova, T. Jungwirth, D.-s. Wang, E. Wang, and Q. Niu, First Principles Calculation of Anomalous Hall Conductivity in Ferromagnetic bcc Fe, *Phys. Rev. Lett.* **92**, 037204 (2004).

[12] Z. Fang, N. Nagaosa, K. S. Takahashi, A. Asamitsu, R. Mathieu, T. Ogasawara, H. Yamada, M. Kawasaki, Y. Tokura, and K. Terakura, The Anomalous Hall Effect and Magnetic Monopoles in Momentum Space, *Science* **302**, 92 (2003).

[13] L. Šmejkal, A. H. MacDonald, J. Sinova, S. Nakatsuji, and T. Jungwirth, Anomalous Hall antiferromagnets, *Nat. Rev. Mater.* **7**, 482 (2022).

[14] V. Baltz, A. Manchon, M. Tsoi, T. Moriyama, T. Ono, and Y. Tserkovnyak, Antiferromagnetic spintronics, *Rev. Mod. Phys.* **90**, 015005 (2018).

[15] T. Jungwirth, X. Marti, P. Wadley, and J. Wunderlich, Antiferromagnetic spintronics, *Nat. Nanotechnol.* **11**, 231 (2016).

[16] T. Graf, C. Felser, and S. S. Parkin, Simple rules for the understanding of Heusler compounds, *Prog. Solid State Chem.* **39**, 1 (2011).

[17] J. Kübler and C. Felser, Berry curvature and the anomalous Hall effect in Heusler compounds, *Phys. Rev. B* **85**, 012405 (2012).

[18] L. Wollmann, A. K. Nayak, S. S. Parkin, and C. Felser, Heusler 4.0: Tunable materials, *Annu. Rev. Mater. Res.*

47, 247 (2017).

[19] M. E. Jamer, Y. J. Wang, G. M. Stephen, I. J. McDonald, A. J. Grutter, G. E. Sterbinsky, D. A. Arena, J. A. Borchers, B. J. Kirby, L. H. Lewis, B. Barbiellini, A. Bansil, and D. Heiman, Compensated Ferrimagnetism in the Zero-Moment Heusler Alloy Mn_3Al , *Phys. Rev. Appl.* **7**, 064036 (2017).

[20] M. Park, G. Han, and S. H. Rhim, Anomalous Hall effect in a compensated ferrimagnet: Symmetry analysis for Mn_3Al , *Phys. Rev. Res.* **4**, 013215 (2022).

[21] W. Shi, L. Muechler, K. Manna, Y. Zhang, K. Koepernik, R. Car, J. van den Brink, C. Felser, and Y. Sun, Prediction of a magnetic Weyl semimetal without spin-orbit coupling and strong anomalous Hall effect in the Heusler compensated ferrimagnet Ti_2MnAl , *Phys. Rev. B* **97**, 060406 (2018).

[22] Y. Zhang, Y. Sun, H. Yang, J. Železný, S. P. P. Parkin, C. Felser, and B. Yan, Strong anisotropic anomalous Hall effect and spin Hall effect in the chiral antiferromagnetic compounds Mn_3X ($X = Ge, Sn, Ga, Ir, Rh$, and Pt), *Phys. Rev. B* **95**, 075128 (2017).

[23] L. Šmejkal, R. González-Hernández, T. Jungwirth, and J. Sinova, Crystal time-reversal symmetry breaking and spontaneous Hall effect in collinear antiferromagnets, *Sci. Adv.* **6**, eaaz8809 (2020).

[24] J. Noky, Q. Xu, C. Felser, and Y. Sun, Large anomalous Hall and Nernst effects from nodal line symmetry breaking in Fe_2MnX ($X = P, As, Sb$), *Phys. Rev. B* **99**, 165117 (2019).

[25] P. Li, J. Koo, W. Ning, J. Li, L. Miao, L. Min, Y. Zhu, Y. Wang, N. Alem, C.-X. Liu, Z. Mao, and B. Yan, Giant room temperature anomalous Hall effect and tunable topology in a ferromagnetic topological semimetal Co_2MnAl , *Nat. Commun.* **11**, 3476 (2020).

[26] Z. L. Sun, K. L. Peng, J. H. Cui, C. S. Zhu, W. Z. Zhuo, Z. Y. Wang, and X. H. Chen, Pressure-controlled anomalous Hall conductivity in the half-Heusler antiferromagnet $GdPtBi$, *Phys. Rev. B* **103**, 085116 (2021).

[27] C. Singh, V. Singh, G. Pradhan, V. Srihari, H. K. Poswal, R. Nath, A. K. Nandy, and A. K. Nayak, Pressure controlled trimerization for switching of anomalous Hall effect in triangular antiferromagnet Mn_3Sn , *Phys. Rev. Res.* **2**, 043366 (2020).

[28] R. D. d. Reis, M. Ghorbani Zavareh, M. O. Ajeeesh, L. O. Kutelak, A. S. Sukhanov, S. Singh, J. Noky, Y. Sun, J. E. Fischer, K. Manna, C. Felser, and M. Nicklas, Pressure tuning of the anomalous Hall effect in the chiral antiferromagnet Mn_3Ge , *Phys. Rev. Mater.* **4**, 051401 (2020).

[29] A. S. Sukhanov, S. Singh, L. Caron, T. Hansen, A. Hoser, V. Kumar, H. Borrman, A. Fitch, P. Devi, K. Manna, C. Felser, and D. S. Inosov, Gradual pressure-induced change in the magnetic structure of the noncollinear antiferromagnet Mn_3Ge , *Phys. Rev. B* **97**, 214402 (2018).

[30] S. Kim, S. Pathak, S. H. Rhim, J. Cha, S. Jekal, S. C. Hong, H. H. Lee, S.-H. Park, H.-K. Lee, J.-H. Park, S. Lee, H.-G. Steinrück, A. Mehta, S. X. Wang, and J. Hong, Giant Orbital Anisotropy with Strong Spin-Orbit Coupling Established at the Pseudomorphic Interface of the Co/Pd Superlattice, *Adv. Sci.* **9**, 2201749 (2022).

[31] J. Son, S. Lee, S. J. Kim, B. C. Park, H.-K. Lee, S. Kim, J. H. Kim, B. H. Hong, and J. Hong, Hydrogenated monolayer graphene with reversible and tunable wide band gap and its field-effect transistor, *Nat. Commun.* **7**, 13261 (2016).

[32] G. Kresse and J. Furthmüller, Efficient iterative schemes for ab initio total-energy calculations using a plane-wave basis set, *Phys. Rev. B* **54**, 11169 (1996).

[33] J. P. Perdew, K. Burke, and M. Ernzerhof, Generalized Gradient Approximation Made Simple, *Phys. Rev. Lett.* **77**, 3865 (1996).

[34] X. Wang, J. R. Yates, I. Souza, and D. Vanderbilt, Ab initio calculation of the anomalous Hall conductivity by Wannier interpolation, *Phys. Rev. B* **74**, 195118 (2006).

[35] I. Souza, N. Marzari, and D. Vanderbilt, Maximally localized Wannier functions for entangled energy bands, *Phys. Rev. B* **65**, 035109 (2001).

[36] S. S. Tsirkin, High performance Wannier interpolation of Berry curvature and related quantities with Wannier-Berry code, *npj Comput. Mater.* **7**, 33 (2021).

[37] See Figs. S1 and S2 of Supplemental Material at <http://link.aps.org/supplemental/xxxxxx>. Spin resolved band structure with and without strains are shown. At Γ , the half-metallicity is robust while the size of band gap changes.

[38] See Fig. S8 of Supplemental Material at <http://link.aps.org/supplemental/xxxxxx>. For this chemical potential shift, negative charge of 1.52 is needed.

[39] Similar feature is found for opposite chemical potential shift, $\mu = E_F + 0.12$ eV, where the magnitude of AHC monotonically decreases, or σ_{xy} increases from -680 to -292 S/cm with strain. This is not by topological singularity but by band splitting associated with representation near L . See Sec. V of Supplemental Material at <http://link.aps.org/supplemental/xxxxxx>.

[40] See Sec. III of Supplemental Material at <http://link.aps.org/supplemental/xxxxxx>. Fermi surface sheets under different strains are shown for +1% interval, where the Fermi surface contour exhibits smoother and more continuous evolution.

[41] See Fig. S7 of Supplemental Material at <http://link.aps.org/supplemental/xxxxxx>. Bands around $E_F - 0.3$ eV, near nodal lines do not change with respect to strain.

[42] See Fig. S5, and S6 of Supplemental Material at <http://link.aps.org/supplemental/xxxxxx>. For other strains, the overall Berry curvature distribution is similar with different magnitudes.